J. Phys. B: At. Mol. Opt. Phys. **42** (2009) 215202 (13pp) doi:10.1088/0953-4075/42/21/215202

Resonance structure in electron–N_2 scattering around 11.5 eV: high-resolution measurements, *ab initio* calculations and line shape analyses

T H Hoffmann[1,2], M Allan[2], K Franz[1], M-W Ruf[1], H Hotop[1], G Sauter[3] and W Meyer[3]

[1] Fachbereich Physik, Technische Universität KL, 67653 Kaiserslautern, Germany
[2] Department of Chemistry, University of Fribourg, 1700 Fribourg, Switzerland
[3] Fachbereich Chemie, Technische Universität KL, 67653 Kaiserslautern, Germany

Received 30 July 2009, in final form 1 September 2009
Published 27 October 2009
Online at stacks.iop.org/JPhysB/42/215202

Abstract
Using two different experimental setups with energy widths of about 6 and 13 meV, we obtained significantly improved results for the energy dependence of angle-differential (10°–180°) elastic and vibrationally inelastic cross sections for electron scattering from N_2 molecules in the energy range around the narrow $N_2^-\left(R^2\Sigma_g^+\right)$ resonance. The energy location and the natural width of this resonance are determined as 11.497(2) eV and 1.3(2) meV, respectively. *Ab initio* potential energy curves are obtained from CCSD(T) calculations for the neutral $N_2\left(X^1\Sigma_g^+\right)$ and $N_2^*\left(E^3\Sigma_g^+\right)$ states as well as for the $N_2^-\left(R^2\Sigma_g^+\right)$ resonance state. They corroborate quite accurately the measured resonance energy and provide accurate energy spacings and overlap integrals for the pertinent vibrational states. A detailed analysis of resonance line shapes for selected scattering angles is performed by applying a model for the interference of resonant and nonresonant scattering processes. It provides a link between the resonance width to absolute DCS and describes elastic and vibrational excitation processes on a common basis. Through both their size and sign, vibrational overlap integrals are shown to determine the observed Fano-type line shapes and account for the opposite asymmetries and intensity changes of adjacent vibrational resonance peaks. Fine-tuning of the fits to the observed shapes is achieved by proper parametrization of the nonresonant amplitudes. A highly resolved excitation function for the formation of the metastable $N_2^*(E^3\Sigma_g^+)$ level from threshold (near 11.88 eV) to 13.4 eV is also presented.

(Some figures in this article are in colour only in the electronic version)

1. Introduction

A sharp resonance in electron scattering from ground state $N_2\left(X^1\Sigma_g^+, v=0\right)$ molecules was first reported by Heideman *et al* [1]; in an electron transmission experiment (energy width $\Delta E = 50$ meV), they located the resonance at 11.48(5) eV and gave an upper limit of 20 meV for its width Γ. Subsequently, Comer and Read [2] performed an angle-differential electron scattering experiment ($\Delta E = 40(5)$ meV) in which the elastic ($\Delta v = 0$) and the vibrationally inelastic ($\Delta v = 1, 2, 3$) processes were studied. From a detailed analysis of the resonance in elastic scattering at $\theta = 40°$ and the near-isotropic angular distribution of vibrational inelastic scattering, Comer and Read concluded that the symmetry of the resonance (subsequently labelled by the letter R) is $^2\Sigma_g^+$ and proposed that the most likely parent state is the $E^3\Sigma_g^+$ state at 11.87 eV [3]. Thus the leading configuration of the resonance state can be written as $2\sigma_g^2\,2\sigma_u^2\,1\pi_u^4\,3\sigma_g^1\,4\sigma_g^2$. Moreover, they estimated the resonance width Γ as 0.6 meV. The $N_2^-\left(R^2\Sigma_g^+, v=0\right)$ resonance was also observed by Kisker

[4] as a small peak in the excitation function of the $N_2(C^3\Pi_u)$ state ($\Delta E = 50$ meV), in the excitation function of the $N_2(B^3\Pi_g)$ state ($\Delta E = 30$ meV) by Mazeau *et al* [5] and in transmission experiments by Sanche and Schulz [6] and by Golden *et al* [7]. In 1973, Schulz [8] reviewed the knowledge achieved to that date.

A high-resolution study of the $N_2^-\left(R^2\Sigma_g^+\right)$ resonance in elastic scattering at $\theta = 22^\circ$ was carried out by van Brunt and Gallagher, who used a laser photoelectron source (apparent resonance width 12 meV, see figure 6 in [9]). Newman *et al* [10] reported the first observation of this narrow resonance in the yield for formation of metastable excited N_2 levels and positioned the $v = 0$ and $v = 1$ states of the resonance at 11.499(10) eV and 11.770(10) eV. Later, angular resolved vibrational excitation (VE) of N_2 ($\Delta v = 1$) through this resonance was restudied by Tremblay and Roy [11] over the range $\theta = 18^\circ$–162° with improved resolution ($\Delta E \approx 25$ meV). They found that the ratio of the intensities for VE via the $v = 0$ and the $v = 1$ resonances was smaller than unity and nearly constant at angles below 122°, but changed 'quite dramatically at larger angles, the first peak becoming increasingly higher than the second peak' [11]. This observation was interpreted as an interference effect between the resonant and the nonresonant amplitudes. Quite recently, another elastic scattering study of the $N_2^-\left(R^2\Sigma_g^+\right)$ resonance was carried out by Mielewska *et al* ($\Delta E = 35$ meV) [12], who used a magnetic angle changer [13] to extend the angular range to 180°.

In the present work, two different experimental setups have been used to restudy elastic and vibrationally inelastic electron scattering from N_2 molecules in the energy range around 11.5 eV at improved energy resolution ($\Delta E \approx 6$ and 13 meV, respectively). Moreover, we report a highly resolved excitation function ($\Delta E \approx 6$ meV) for the formation of the metastable $N_2^*(E^3\Sigma_g^+)$ level near threshold. To aid the interpretation of the experimental data, high level *ab initio* calculations of the relevant potential energy curves have been carried out. The resonance spectra are analysed using an ansatz which incorporates the important interfering scattering paths.

The paper is organized as follows. In section 2, we briefly describe the two experiments in Kaiserslautern (referred to as KL) and Fribourg (referred to as FR); in section 3, we sketch the *ab initio* calculation of the potential energy curves for $N_2\left(X^1\Sigma_g^+\right)$, $N_2^*\left(E^3\Sigma_g^+\right)$ and $N_2^-\left(R^2\Sigma_g^+\right)$ and compare with spectroscopic data. Section 4 provides some background for the modelling of resonance line shapes as applied here. In section 5, we present the experimental results and their analyses and compare with previous results. We conclude with a brief summary.

2. Experimental

2.1. Experiment at Kaiserslautern

Potassium atoms in a collimated atomic beam are photoionized at threshold by a two-step process via the $K(4p_{3/2})$ level [14], using a stabilized two-frequency Ti:Sa laser ($\lambda_1 = 767$ nm) for excitation and a focused intracavity dye laser ($\lambda = 455$ nm) for ionization (see figure 1). The near-zero energy photolectrons are extracted by a weak electric field ($\approx 10\,\mathrm{V\,m^{-1}}$) and imaged onto the target beam. Five retarding field electron detectors at fixed angles count the scattered electrons (only that at 90° is shown), such that both truly elastic and rotationally inelastic/superelastic processes are sampled with equal probability. The triply differentially pumped supersonic target beam nearly eliminates Doppler broadening [15–17]. To correct for background electrons, alternating measurements with and without target beam were carried out and the latter spectra subtracted from the former. The background amounted to about 20% at 22.5° and 135° and around 10% for the other angles. Drifts of the energy scale were accounted for by passive spectrum stabilization, as described in [16, 17]. At a beam current of 80 pA, an energy width of about 6 meV was obtained. The angular distribution for elastic scattering at energies close to, but not coinciding with the resonance, was found to be independent (to within 10%) of stagnation pressure over the range 1–6 bar and to agree with that measured with the Fribourg instrument to within 20% or better.

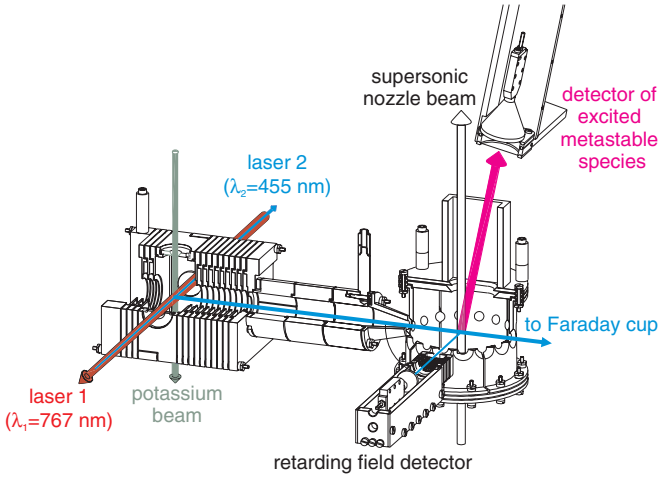

Figure 1. Kaiserslautern laser photoelectron source setup for high-resolution measurements of elastic scattering; only one of the five detectors for elastically scattered electrons is shown (22.5°, 45°, 90° (in figure), 112.5°, 135°).

The production of long-lived excited species is monitored by a channel electron multiplier, mounted slightly off the direction of the target beam, to account for the momentum transfer induced by the excitation process.

2.2. Experiment at Fribourg

Electrons emitted from a hot filament are energy selected by a double hemispherical monochromator and focused onto an effusive beam target, introduced by a 0.25 mm nozzle kept at about 30 °C (see figure 2). A double hemispherical analyser for detection of elastically or inelastically scattered electrons ensures background-free signals [18]. Monochromator and analyser are operated at equal pass energy and provide the same energy resolution. Absolute cross sections are determined by comparison against He using a relative flow method [19]. A specially designed magnetic angle changer

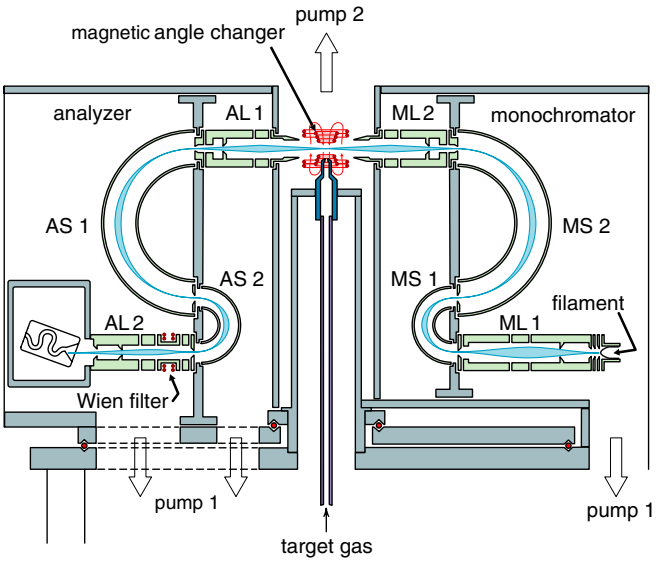

Figure 2. Fribourg electron scattering apparatus involving double hemispherical monochromator and analyser.

allows for continuously sweeping the angle and in particular measurements up to 180° scattering angle [20]. Detailed procedures for ensuring reliable cross sections have been described elsewhere [21, 22]. The accuracy is about ±15% for the elastic cross sections and ±20% for the vibrationally inelastic cross sections. The energy width of the incident electron beam was around 13 meV at a current of about 400 pA. Some measurements at 30°, 45° and 90° were performed with a resolution around 10 meV. The analyser, when set to the centre of the respective vibrational scattering peak ($\Delta v = 0 - 3$), preferentially detects rotational processes with $\Delta J = 0$ (for $J = 7$, the most populated level at 300 K, *S*-branch ($\Delta J = +2$) and *O*-branch ($\Delta J = -2$) scattering are displaced from the rotationally elastic *Q*-branch ($\Delta J = 0$) by −8.5 meV and +6.5 meV, respectively).

3. CCSD(T) calculations and comparison with spectroscopic data

For the ground state $N_2(X^1\Sigma_g^+)$, the excited state $N_2^*(E^3\Sigma_g^+)$—which is the parent state of the resonance—and the resonance state $N_2^-(R^2\Sigma_g^+)$, *ab initio* potential curves were determined in CCSD(T) calculations using the MOLPRO program package [23]. The coupling of the resonance state to its embedding continuum is sufficiently weak that these calculations converge nicely without any help from a projection algorithm. Due to small excitation energies for $4\sigma_g^2 \rightarrow 2\pi_u^2$, the norm of the T_2 part of the CC wavefunction does increase from 0.12 for the X state to 0.23 for the R state. This is still acceptable, so that the CC calculations can be trusted over the range of internuclear distances relevant here. Of course, an adequate treatment of the resonance state requires augmenting the standard cc-aVQZ basis set (library of MOLPRO [23]) by several sets of diffuse functions. A graphical representation of the potential curves (*ab initio* energy points with fitted Morse potential curves) is shown in figure 3.

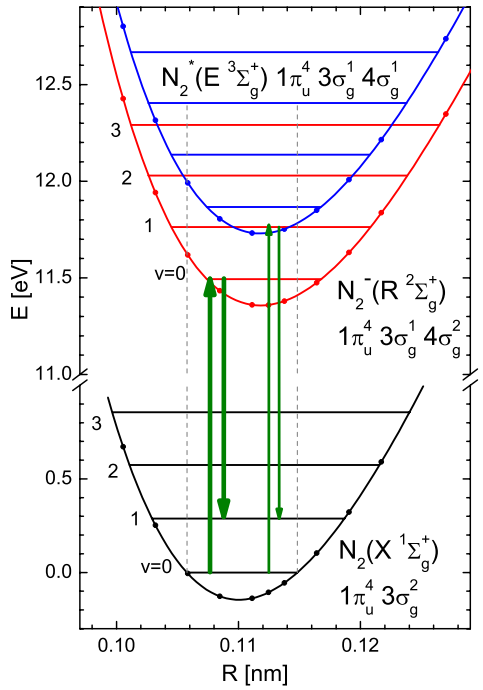

Figure 3. *Ab initio* potential curves for the $N_2(X^1\Sigma_g^+)$ ground state, the $N_2^*(E^3\Sigma_g^+)$ parent state and the $N_2^-(R^2\Sigma_g^+)$ resonance with respective dominant configuration, Franck–Condon region indicated by dashed lines; the arrows indicate the pathways for resonant vibrational excitation of $N_2(X^1\Sigma_g^+, v = 1)$.

Vibrational levels were obtained with the Numerov method. The calculated spectroscopic constants are given in table 1 and are seen to agree nicely with experimental data for the X and E states, respectively. We expect a similar accuracy for the R state as well, but the nearly perfect agreement of calculated and measured resonance positions (T_{00} of table 1) is certainly somewhat fortuitous. The resonance state, its parent state and the cation ground state have all virtually the same equilibrium internuclear separations and very similar vibrational frequencies, as expected from the weak interaction of the outer shell $4\sigma_g^2$ electron pair with the cationic electron core. These separations are only slightly larger than that of the $N_2(X^1\Sigma_g^+)$ ground state, reflecting the only weakly bonding nature of the $3\sigma_g$ orbital which may be characterized as a linear combination of the two localized lone-pair orbitals of N_2. From the orbital angular momentum expectation value $\langle 3\sigma_g|l^2|3\sigma_g\rangle = 3.40$ we infer an approximate partial wave decomposition of $3\sigma_g \approx 0.75\text{s} + 0.65\text{d} + 0.20\text{g} + \cdots$. The outer electron pair of the resonant state may be characterized by its configuration expansion, $0.80\ 4\sigma_g^2 - 0.46\ 5\sigma_g^2 - 0.08\ ^3(4\sigma_g 5\sigma_g) - 0.21\ 3\sigma_u^2 - 0.23\ (2\pi_{ux}^2 + 2\pi_{uy}^2)$, and the fact that $4\sigma_g$ and $5\sigma_g$ are nearly pure s orbitals. Its radial extension may be quantified by $\left[\langle\psi_R|\sum r_i^2|\psi_R\rangle/2\right]^{1/2} = 7.4$ Bohr. This is rather similar to what has been found for the corresponding resonance state of Ar. The leading coupling term between resonance state and the corresponding continuum is given by the two-electron integral $\langle 4\sigma_g(1)4\sigma_g(2)|r_{12}^{-1}|3\sigma_g(1)\epsilon\sigma_g(2)\rangle$, so that the partial wave decomposition of the continuum orbital $\epsilon\sigma_g$ reflects closely that of the orbital $3\sigma_g$.

Table 1. Spectroscopic constants for the pertinent electronic states of $^{14}N_2$; T_{00}: transition energies between rovibrational ground states. [a]Present *ab initio* calculation, [b]experimental values [24], [c][25] (B_e obtained from experimental $B_0 = 1.9273\ cm^{-1}$ using calculated rovibrational coupling constant $\alpha_e(E) = 0.0181\ cm^{-1}$; ω_e inferred from $\omega_0 = 2185$ using calculated anharmonicity) and [d]present experiment.

State	R_e (Å)	B_e (cm^{-1})	ω_e (cm^{-1})	$\omega_e x_e$ (cm^{-1})	$\omega_e y_e$ (cm^{-1})	T_{00} (eV)
$N_2(X^1\Sigma_g^+)^a$	1.1004	1.9883	2356.6	15.47	−0.503	
$N_2(X^1\Sigma_g^+)^b$	1.0977	1.9982	2358.5	14.32	−0.002	
$N_2^*(E^3\Sigma_g^+)^a$	1.1181	1.9261	2216.9	16.08	−0.477	11.866
$N_2^*(E^3\Sigma_g^+)^c$	1.1151	1.9364	2219			11.874
$N_2^-(R^2\Sigma_g^+)^a$	1.1182	1.9255	2207.7	14.93	−0.897	11.493
$N_2^-(R^2\Sigma_g^+)^d$			2205(10)	15(5)		11.497(2)
$N_2^+(X^2\Sigma_g^+)^a$	1.1187	1.9237	2206.5	15.70	−0.606	15.551
$N_2^+(X^2\Sigma_g^+)^b$	1.1164	1.9318	2207.00	16.10	−0.040	15.581

Table 2. Vibrational overlap integrals for rotationless states of $N_2(X^1\Sigma_g^+)$ and $N_2^-(R^2\Sigma_g^+)$.

v_R/v_X	0	1	2	3
0	0.9620	−0.2693	0.0458	−0.0058
1	0.2659	0.8846	−0.3741	0.0815
2	0.0611	0.3648	0.8038	−0.4497
3	0.0135	0.1052	0.4331	0.7178

The resonance width is much smaller than the separation of vibrational levels in the resonance potential, and thus these levels are well defined. Under these conditions, as discussed by Comer and Read [26], the cross section for resonant vibrational excitation from an initial vibronic level (X, v_i) to a final level (X, v_f) via the resonance level (R, v) is proportional to the product of the two pertaining transition probabilities. The latter can be well represented by a common prefactor and v-dependent Franck–Condon factors, due to the small amplitude of the vibrational motion. Accordingly, the corresponding amplitude for vibrational excitation, which governs the interference of direct and resonant processes, is proportional to the product of the pertaining vibrational overlap integrals. These integrals, as calculated from our *ab initio* potentials, are collected in table 2. The signs of the vibrational wavefunctions are fixed by requiring a positive start at small R.

Vibrational excitation of ground state N_2 to a particular final state v_f may proceed via different pathways, depending on the intermediate vibrational state of the resonance. This is indicated for $v_f = 1$ by arrows in figure 3. These processes show up as separate resonance peaks with line shapes that are related by the fact that the interference with the (more or less) same non-resonant background is mainly modulated by the products of vibrational overlap integrals.

4. Analysis of resonance line profiles

The elastic DCSs measured over a dense energy grid around the $N_2^-\left(R^2\Sigma_g^+, v = 0\right)$ resonance position show typical Fano-type line shapes with a dependence on the scattering angle that is reminiscent of the $He^-(1s2s^2\ ^2S_{1/2})$ resonance. In the case of a spherical scatterer, the variation of the resonance profile with angle can be calculated once the phase shifts for direct (nonresonant) scattering and the angular momentum of the resonance are known (see, e.g., [15]). Although the homonuclear diatomic molecule N_2 maintains a high degree of symmetry, the analysis of the angular dependence of the DCS is rather involved. While the fixed-nuclei approximation used for the direct scattering is certainly appropriate there, its validity may be in doubt for resonant scattering. The rotational periods are $\geqslant$3.5 ps for the measurements at KL (mainly $J \leqslant 2$ due to rotational cooling in the supersonic expansion) and about 1 ps for the FR measurements (most populated rotational level $J = 7$), as compared to the lifetime of the resonance of 0.5 ps. But even with this approximation, there is no reliable direct scattering amplitude available in the literature on which we could build an angular analysis of the interference between direct and resonant scattering. Therefore, we focus here merely on a modelling of the energy profiles and the extraction of a reliable value for the resonance width. We take the apparent similarity of the line shapes from the two sets of measurements that differ greatly in their rotational temperatures as a justification for the neglect of rotational motion. We just note that the rotational population distribution causes an inhomogeneous broadening of the resonance even if only $\Delta J = 0$ transitions are involved. With the rotational constants given in table 1 for the X and R states, this broadening—while negligible for the KL experiment—amounts to about 0.5 meV for the FR experiment. But this is still unobservable given the resolution of 12–14 meV.

For convenience, we shall denote the DCS simply by $\sigma(\theta; \epsilon)$ and may even drop the arguments. Its energy dependence in the neighbourhood of an isolated resonance is given by the terms $\sigma_{r0}/(1+\epsilon^2)$ and $\sigma_{r1}\epsilon/(1+\epsilon^2)$ on top of only weakly energy-dependent contributions of nonresonant processes, $\sigma_{nr} = \sigma_{nr0} + \sigma_{nr1}(E - E_r)$. Here, $\epsilon = 2(E - E_r)/\Gamma$ is the usual reduced, dimensionless energy variable. The resonance width Γ is assumed to be independent of scattering angle and energy for the energy interval under investigation. A combination of these terms provides a modelling of the line shapes as proposed by Shore [27]. More popular is the (equivalent) modelling as a Fano profile [28], $\sigma = \sigma_{min} + \sigma_r(q+\epsilon)^2/(1+\epsilon^2)$, but for fitting purposes this has the disadvantage of the shape parameter q tending to infinity (and σ_r to zero) for a symmetric peak. Hence, we follow Andrick

[29] and replace q by $\tan(\beta)$. This leads to an expression which is convenient for a least squares fit of the measured line profiles:

$$\sigma = \sigma_{nr} + \Delta\sigma[-\cos(2\beta) + \sin(2\beta)\epsilon]/(1+\epsilon^2), \quad (1)$$

where $\Delta\sigma = \sigma_{\max} - \sigma_{\min}$ is the size of the line modulation and $\sigma_{\min} = \sigma_{nr} - \Delta\sigma\cos^2(\beta)$ should never be negative. Of course, the fit involves an energy convolution representing the resolution ΔE of the apparatus, as usual accounted for by a Gaussian function. In addition to the four linear parameters of the above model these fits involve as nonlinear parameters the common resonance width Γ and resonance position E_r via ϵ, and the (weakly angular-dependent) FWHM ΔE. As seen in figures 5 and 6, excellent fits of the two sets of experimental data could be achieved, i.e. χ^2 is close to 1 when only statistical errors are attributed to the electron counts. However, it was not possible to determine Γ and ΔE separately from the line shapes: even with an energy width as low as 6 meV, χ^2 of the fit turned out insensitive to the difference $\Gamma - \Delta E$ for a range well over 1 meV. Only lower bounds for Γ could be derived from the requirement that ΔE should not take values which imply a negative $\sigma_{\min}$: for the FR measurements, $\sigma_{\min}$ of $\theta = 180^\circ$ turns negative below $\Gamma = 1.25$ meV; for the KL measurements, $\sigma_{\min}$ of $\theta = 135^\circ$ turns negative below $\Gamma = 1.15$ meV. Since independent and sufficiently accurate measurements of the resolution were not possible, a reliable value for Γ can only be derived by reference to the absolute DCS obtained in the FR measurements. To this end, the line shapes need to be related to physical parameters of the resonant and non-resonant interactions. We assume that the resonance interferes only with a single non-resonant process and apply the ansatz

$$\sigma_v(\theta;\epsilon) = |2t(v)p(\theta)/(\epsilon+\mathrm{i}) + a(\theta)\,\mathrm{i}\,\mathrm{e}^{-\mathrm{i}\phi(\theta)}|^2/(4k_\mathrm{i}k_\mathrm{f}), \quad (2)$$

where k_i and k_f are the momenta of the incident and the scattered electrons, respectively. A similar ansatz has already been used by Comer and Read [2] and later also by Tremblay and Roy [11] in the analysis of their measurements on the same topic. It can be derived from the general structure of the T matrix, see e.g. Burke [30], and has been shown by Andrick [29] to conform with the common phase shift analysis of DCS in atomic scattering. Comparison with the above defined line shape model gives the relations

$$a^2 = 4k_\mathrm{i}k_\mathrm{f}\sigma_{nr}, \quad (3)$$

$$(2t(v)p(\theta))^2 = 4k_\mathrm{i}k_\mathrm{f}\left(\sigma_{\max}^{1/2} \pm \sigma_{\min}^{1/2}\right)^2 = 4k_\mathrm{i}k_\mathrm{f}\sigma_{pr}, \quad (4)$$

$$\sin(\phi) = \sin(2\beta)4k_\mathrm{i}k_\mathrm{f}\Delta\sigma/(4at(v)p(\theta)). \quad (5)$$

The factor $\mathrm{i}\,\mathrm{e}^{-\mathrm{i}\phi}$ accounts for the phase difference of the resonant and non-resonant processes. The factor $t(v)$ represents the product of vibrational overlap integrals, $t_{v_\mathrm{f},v_\mathrm{r}}t_{v_\mathrm{r},v_\mathrm{i}}$, involved in the resonant scattering from the initial state (X, v_i) to the final state (X, v_f) via the resonance state (R, v_r). The function $p(\theta)$ reflects the (effective) angular characteristics of the resonance. An important point is that $p(\theta)^2/2$ should be a normalized angular distribution in the case that the interaction which causes the resonance profile is also the one by which the unperturbed resonance decays, i.e. which determines the width of the resonance. Since this is valid here it opens the way to derive Γ from absolute DCS via angular integration of $p(\theta)^2$. The hypothetical 'pure resonant' DCS $\sigma_{pr}(\theta)$ defined in equation (4) serves mainly for a convenient comparison with experimental DCS and fit parameters $\Delta\sigma$, $\sigma_{\min}$ etc. Due to the splitting of the resonance amplitude into factors $t(v)$ and $p(\theta)$ we expect this ansatz to provide a proper basis for a common interpretation of the line shapes from our elastic and vibrational excitation cross section measurements.

Another point not yet touched upon is rotational excitation in (the nominally) elastic and vibrationally inelastic scattering. So far, this aspect has been only addressed experimentally in the work of Gote and Ehrhardt [31]. At the incident energy $E = 10$ eV, they concluded from simulations of the line shapes of $\Delta v = 0$ energy loss spectra that $\Delta J = 0$ processes are dominant up to 70°, while for larger angles $\Delta J = \pm 2$ processes are strongest. A substantial contribution of $\Delta J = \pm 2$ processes to nonresonant scattering would provide a background that does not interfere with resonant scattering if the latter only involves $\Delta J = 0$ processes. This is what we find in resonant vibrational excitation, in line with observations for the (admittedly rather different) case of vibrational excitation of H_2 via the sharp $H_2^-\left(^2\Sigma_g^+\right)$ Feshbach resonance, for which Linder and Schmidt have shown that only $\Delta J = 0$ rotational transitions contribute [32], in contrast to their observations for direct excitation. In the case of elastic scattering we observe very deep modulation of the DCS in particular for larger angles where little space is left for non-interfering background in our model. This seems to indicate similar interference also in the rotational excitation channels. But lacking stringent evidence for rotational excitation in the elastic channel, we decided to ignore its effect at present and assume zero non-interfering background in elastic scattering.

5. Experimental results and discussion

5.1. Nonresonant scattering

The angular distribution of electrons scattered elastically from N_2 was measured at an incident energy of 11.4 eV (0.1 eV below the $N_2^-\left(R^2\Sigma_g^+\right)$ resonance) by magnetically scanning the angle in three intervals around 45°, 90° and 135°, as described in [21]. They were merged in accordance with separately measured absolute differential cross sections at several angles, given in table 3. Either by scanning the residual energy at constant incident energy and integrating over peak areas or by comparing count rates under identical conditions, cross sections for vibrational excitation were also brought to an absolute scale. As expected in view of the absence of infrared active vibrations, nonresonant contributions to VE are weak and likely enhanced by adjacent broad resonances, as discussed at the end of section 5.3. All absolute DCSs are collected in table 3.

Our absolute differential cross section for elastic scattering of electrons from N_2 at $E = 11.4$ eV is shown in figure 4. For lack of other data at this energy, comparison is made with previous experimental and theoretical data for $E = 10$ eV [31, 33–36]. In order to indicate what changes are

Table 3. Absolute differential cross section for elastic and inelastic scattering of electrons from N_2 at an incident energy $E = 11.4$ eV; accuracy ±15% for elastic and ±20% for inelastic scattering.

Angle (°)	10.0	22.5	45.0	90.0	112.5	135.0	180.0
Elastic (10^{-20} m^2 sr^{-1})	3.32	2.38	1.43	0.33	0.47	0.69	0.92
$v = 1$ (10^{-24} m^2 sr^{-1})	25.0	10.6	11.0	5.0	2.8	4.2	21.6
$v = 2$ (10^{-24} m^2 sr^{-1})	1.4	1.2	0.43	0.44	0.44	0.86	2.1

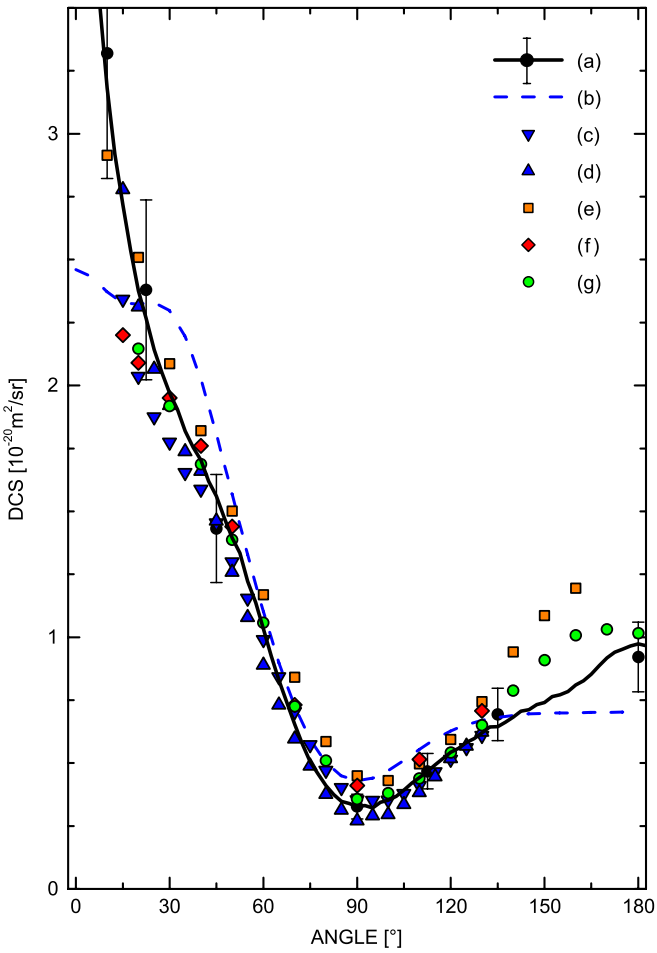

Figure 4. Differential cross section for elastic scattering near the resonance. (a) Present experiment at an incident energy of 11.4 eV; individual absolute cross sections are indicated as solid circles with error bars; (b) Theoretical data from Sun *et al* [33], calculated for 10 eV; (c) measurement from Sun *et al* at 10 eV; (d) experimental data from Sun *et al* extrapolated to 11.4 eV; (e) measurement from Gote and Ehrhardt [31] at 10 eV; (f) experimental data from Muse *et al* [34] at 10 eV; (g) measurement from Linert and Zubek [35] at 10 eV.

to be expected when going from 10 eV to 11.4 eV, we include the result from a linear extrapolation of the cross section given in [33] for 8 eV and 10 eV (even though there seems to be no simple trend from 6 eV to 10 eV). Agreement between the present measurements and these extrapolated data is seen to be very satisfactory, given the uncertainties allowed for both experiments. Recent data from Muse *et al* [34] exhibit a similar shape of the cross section. The measurements of Gote and Ehrhardt [31] differ significantly only in the range from 140° to 160°, where they are more akin to the earlier results of Shyn and Carignan [37]. The recently reported DCSs of Linert and Zubek [35] are in very good agreement with our results from 20° to 130°; at larger angles up to 180° they lie between 5% and 20% above our values. In view of the agreement between our recent large-angle scattering data for rare gas targets and corresponding theory [38], we are rather confident of our data between 135° and 180°. They appear to be supported also by the calculations of Sun *et al* [33]. These theoretical results, on the other hand, seem to be deficient mainly in the angular range below 40° where they show a distinct shoulder. This is somewhat surprising since forward scattering is dominated by the effects of the long-range interaction potential due to quadrupole moment and dipole polarizability, which have been claimed to be adequately accounted for by numerical Born completion up to electron angular momenta $l_{max} = 12$ in a partial waves expansion up to $L_{max} = 14$ [33, 36]. A full account by analytical first-order Born completion does actually reduce the DCS at low angles even further and produces a maximum at around 30° [36]. Such a maximum appears in the experimental data at energies from 4 to 7 eV albeit not as strong as predicted by theory [33]. Thus, elastic forward scattering seems to be not fully understood for N_2.

5.2. *The* $N_2^-(R^2\Sigma_g^+)$ *resonance in elastic scattering*

Our energy-variable elastic DCS measurements are presented in figures 5 and 6. They exhibit a pronounced dependence of the resonance profiles on the scattering angle, in qualitative agreement with the earlier findings of Comer and Read [2] but with considerably more detail and accuracy. Note that these figures show relative DCS measurements which have been put on absolute scale by joining their values at 11.4 eV with the absolute DCS given in table 3.

The position of the $N_2^-\left(R^2\Sigma_g^+, v = 0\right)$ resonance was determined as 11.497(2) eV relative to the $Ar^-(3p^5 4s^2\ ^2P_{3/2})$ resonance (located at 11.103(1) eV [17]) by analysing measurements with a mixed Ar–N_2-beam in the KL setup, which lends itself to precise energy calibrations due to the suppression of Doppler broadening and simultaneous measurements at all angles. Previous determinations of the resonance position were made at substantially broader energy widths. They agree with our result within their respective uncertainties, namely 11.48(5) eV [1] and 11.37–11.51 eV [6] (transmission experiments) and 11.499(10) eV [10] (as observed in the excitation function of $N_2^*(B^3\Pi_g)$).

The parameters for the fits of the FR data are collected in table 4 and are shown in figure 7 together with the fit parameters for the KL data. We note that the data for 30° have been obtained in a separate run under improved apparatus conditions that led to a significantly smaller width ΔE. For

Table 4. Parameters of equations (1)–(5) for elastic DCS from the FR measurements; resonance width $\Gamma = 1.38$ meV.

θ (°)	10.0	22.5	30.0	45.0	90.0	112.5	135.0	180.0
ΔE (meV)	16.20	14.50	9.80	12.90	13.00	13.10	12.70	15.30
σ_{nr} (Å^2)	3.368	2.395	1.978	1.423	0.321	0.472	0.701	0.939
$\sigma_{\min}$ (Å^2)	1.537	0.874	0.732	0.604	0.068	0.074	0.098	0.054
$\Delta\sigma$ (Å^2)	2.173	1.567	1.247	0.956	0.331	0.468	0.908	1.423
β (°)	23.4	9.9	2.2	−22.3	−28.8	22.7	35.4	37.9
ϕ (°)	38.9	15.8	3.5	−36.6	−41.6	31.5	47.9	46.4
σ_{pr} (Å^2)	0.471	0.394	0.304	0.222	0.138	0.215	0.477	0.966

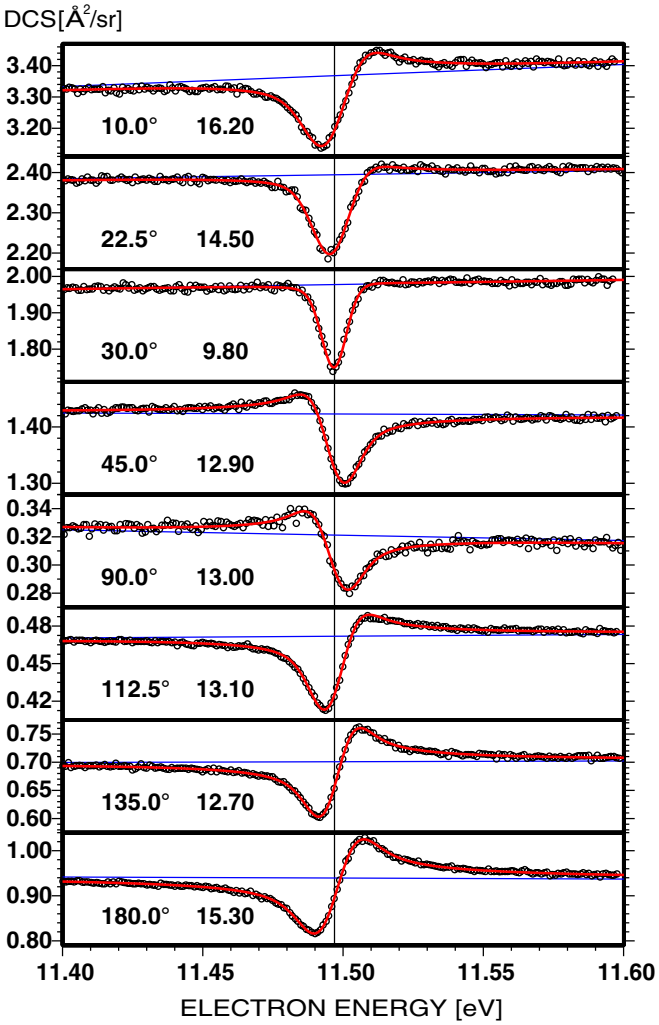

Figure 5. The $N_2^-(R^2\Sigma_g^+)$ resonance as measured with the FR apparatus. The full curve represents fits to the data with resonance width $\Gamma = 1.38$ meV common to all angles. The parameters of the fit are given in table 4; second number in panels gives ΔE in meV.

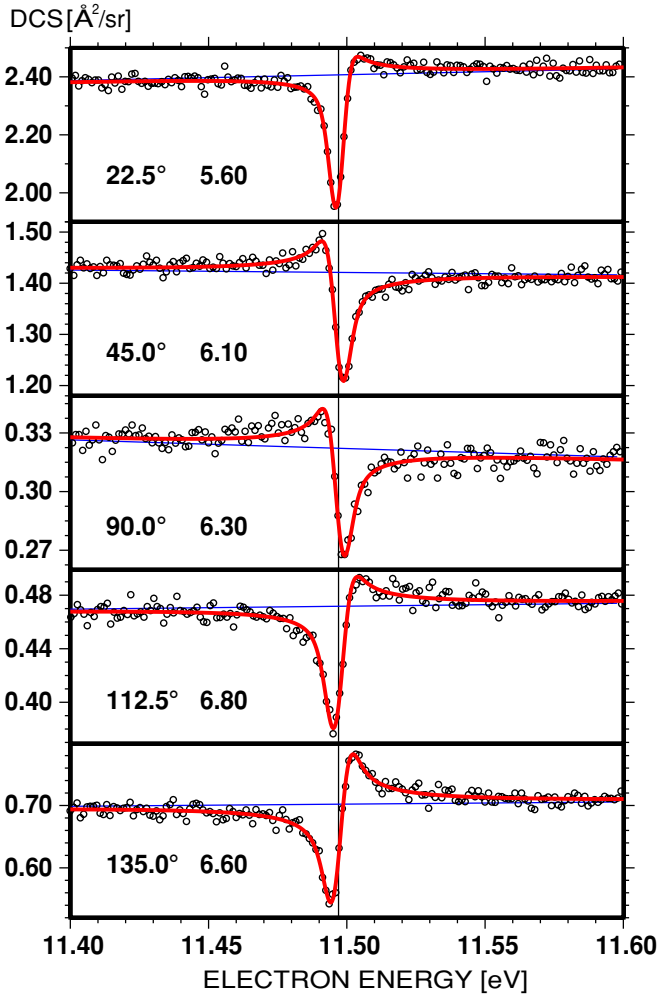

Figure 6. The $N_2^-(R^2\Sigma_g^+)$ resonance as measured with the KL apparatus. The full curve represents fits to the data with resonance width $\Gamma = 1.22$ meV common to all angles; second number in panels gives ΔE in meV.

the other angles ΔE shows a trend as previously observed in analogous measurements for the Ar resonance [17], mainly determined by beam overlap conditions. The shape parameters β are completely independent of the fit parameters ΔE and Γ and thus are very stable parameters. However, without further information on direct and resonant scattering amplitudes we cannot reason about its shape as function $\beta(\theta)$. For σ_{pr} the negative sign in equation (4) has been chosen for reasons of plausibility: with this choice, σ_{pr} is much smaller than σ_{nr} in particular in forward scattering as should be expected from the fact that the interaction with the resonance does not have the long-range tail of the direct interaction; otherwise, σ_{pr} would take values larger than σ_{nr} by factors 2–3. The angular integration of $p(\theta)^2$ has been performed via expansion in terms of Legendre polynomials. This expansion shows dominant terms for $l = 0$ and $l = 2$ as one might expect for a $^2\Sigma_g$ resonance. Somewhat surprisingly, there is also a significant

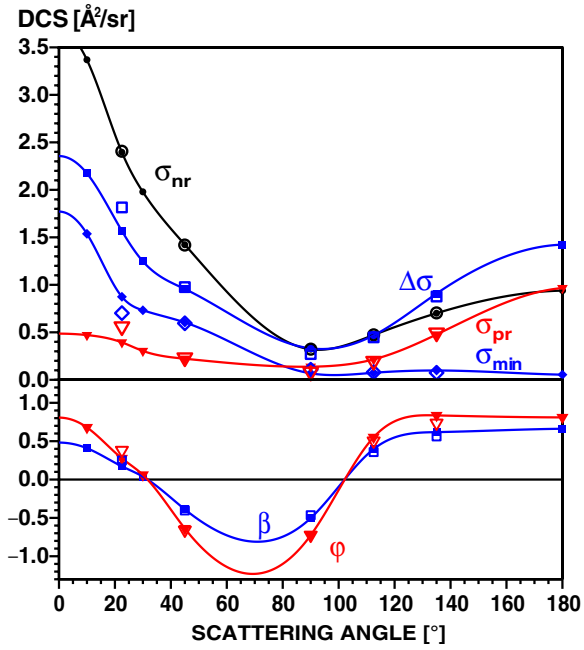

Figure 7. Analysis of elastic DCS measured with the FR (solid points, $\Gamma = 1.38$ meV and the KL (open points, $\Gamma = 1.22$ meV) apparatus, respectively. Solid curves are spline fits to parameters fitting the FR data, see table 4.

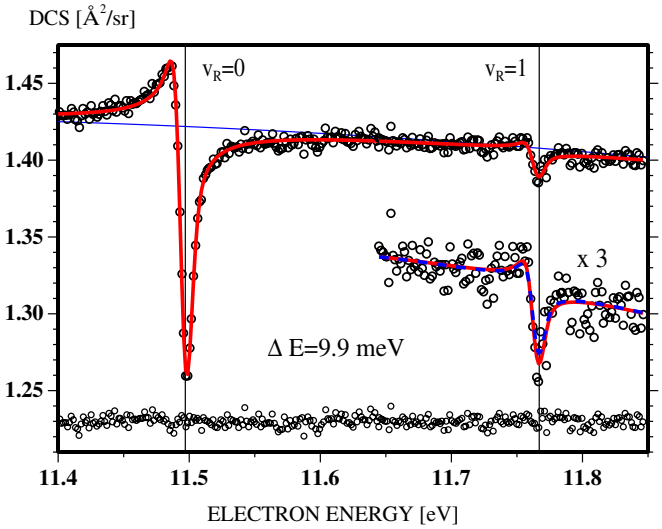

Figure 8. Elastic DCS for $\theta = 45°$ covering the energy range of the $v = 0$ and $v = 1$ resonances. Data points: FR measurements with $\Delta E = 9.9$ meV (from fit of first resonance). Full (red) curve: unconstrained fit of both resonances. Dashed (blue) curve in magnified plot of the $v_R = 1$ resonance: p of equation (2) for the second resonance constrained to its value of the first resonance. Lower set of data: fit errors. (Colour online.)

contribution to σ_{pr} from $l = 1$ due to its relatively large values for backward scattering. The integral of $p(\theta)^2$ hits its theoretical value for $\Gamma = 1.38$ meV and $\Gamma = 1.22$ meV for the FR and KL data, respectively. This difference is not insignificant considering the fact that an uncertainty in the absolute DCS of $\pm 15\%$ translates into an uncertainty of only about $\pm 5\%$ for Γ, if the correlation of Γ with ΔE is taken into account. These Γ values have been chosen for the fitting curves in figures 5, 6 and 8 as well as the parameters of table 4. (Note that there is a strong correlation of Γ not only with ΔE, but also with $\Delta\sigma$ and σ_{pr}). With this choice there is rather good agreement between the two sets of measurements, in particular with respect to the line shape parameters β and ϕ. The largest deviations occur for the angle 22.5° which has a rather small ΔE in the KL measurements.

The smaller value of the width from the KL data may originate from the different ways in which rotational (de)excitation is sampled in the two experiments. If resonant scattering is (predominantly) rotationally elastic ($\Delta J = 0$), $\Delta J = \pm 2$ processes represent noninterfering contributions to the background. $\Delta J = \pm 2$ processes are detected with the same efficiency as $\Delta J = 0$ processes in the KL experiment, while the FR setup discriminates against $\Delta J = \pm 2$ contributions (see section 2). Thus a possible noninterfering background is higher in the KL data, and this may allow for a slightly larger resonance width.

In view of the two concurrent results we propose a resonance width of $\Gamma = (1.3 \pm 0.2)$ meV. Comer and Read suggested a value of only 0.6 meV, mainly based on the resonance dip which they observed at a scattering angle $\theta = 40°$ and which they considered to be purely symmetric. We understand their reasoning for deriving Γ as based on the assumption that $\sigma_{\min}$ reaches zero, which means that their value for Γ should be taken as a lower limit. We note that Comer and Read observed a resonance dip of 2.2% depth, which is the result obtained by convolution of a 0.6 meV wide fully modulated window resonance with a Gaussian resolution function of the quoted 40 meV width. Actually, from the shape parameters β for angles 22.5° and 45° we deduced that a symmetric window peak ($\beta = 0$) should appear close to 30° (see figure 7) and found this verified in the later measurement at that angle.

Elastic scattering may alternatively involve intermediate excitation of the vibrational level $v_R = 1$ of the resonance state. Since the vibrational factor $t(v)$ in equation (2) is reduced from 0.9262 for the main resonance peak to 0.0707 for its higher satellite, the interference term which is linear in $t(v)$ becomes dominant and should account for a satellite peak with a size reduced to about 10%. This was indeed observed in the total cross section from transmission experiments [1, 8] and has also been seen in elastic and inelastic DCS (e.g. Comer and Read). For the selected angle $\theta = 45°$ we have recorded elastic DCS over an energy range encompassing both resonances, as shown in figure 8. As for the 30° measurement, improved apparatus conditions led to a resolution of only 9.9 meV. Reassuringly, the line parameters $\Delta\sigma$ and β for the first resonance kept to within 4% to their values given in table 4. An unconstrained fit of the second resonance led to a strength parameter $p(45°)$ about 15% larger than for the first resonance. Due to the unfavourable signal-to-noise ratio this result is not really significant: the inset in figure 8 shows also a fit where p was constrained to its value for the first resonance, which appears to be perfectly acceptable. Since $\Delta\sigma$ is rather uniformly reduced to 9–10% for all θ, this reduction applies also to the total cross section, in good agreement with observation in [6, 8].

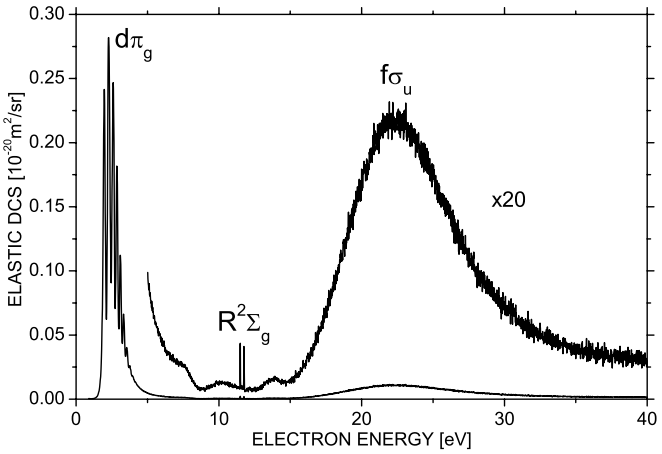

Figure 9. Overview of absolute DCS for vibrational excitation $N_2(X,v = 0 \rightarrow 1)$ over a wide incident electron energy range, measured at a scattering angle of 135°.

5.3. Vibrational excitation

The $N_2^-\left(R^2\Sigma_g^+\right)$ resonance produces striking sharp features in vibrational excitation of the electronic ground state [2, 11]. In figure 9, the DCS for VE at an angle of 135° is shown over a wide energy range up to an energy of 40 eV. The DCS for VE is dominated by resonances over the whole energy range, with the $d\pi_g$ and $f\sigma_u$ shape resonances being most prominent. Adjacent to the narrow $N_2^-\left(R^2\Sigma_g^+\right)$ resonances, there are two small resonance features around 10.2 eV and 13.8 eV.

Absolute DCSs for direct excitation processes at the energy 11.4 eV have been given in table 3. For $\Delta v = 1$, they are about 3 orders of magnitude smaller than the direct elastic DCS, roughly in accord with a transition probability reduced by the factors $\langle 0|R|1\rangle^2 = 3.6 \times 10^{-3}$ from vibrational integration and $[\mathrm{d}\ln(\alpha)/\mathrm{d}R]^2 = 0.25$ or $[\mathrm{d}\ln(q)/\mathrm{d}R]^2 = 0.81$ as the computed ratios of the long-range coupling strength for vibrational excitation and elastic scattering, respectively (α: isotropic dipole polarizability, q: quadrupole moment). The resonant process, on the other hand, should be reduced only according to the ratio of the Franck–Condon factors involved, i.e. by about 1/16. Thus the resonance peaks are expected to be clearly stronger than the nonresonant background and to exhibit a nearly symmetric peak shape. Moreover, any asymmetry should be of opposite direction for the first peak (excitation via (R, $v = 0$) and the second peak (excitation via (R, $v = 1$)). This is indeed what is seen in figure 10 which shows DCS measurements for $\Delta v = 1$ with the FR apparatus. From the Franck–Condon factors and symmetry properties of the involved states, one might further expect nearly isotropic scattering with a ratio of 1.2 between the area of the two peaks. In these respects, the measurements show marked deviations: the area ratio stays nearly constant around 0.8 for angles up to 120° but grows strongly to 3.5 in backward scattering (180°), reflecting a near collapse of the second peak. These dependences of peak areas and peak shapes on scattering angle were already observed and characterized by Tremblay and Roy [11] in measurements over the angular range 18°–162°. They attributed both features to interference between resonant and nonresonant vibrational excitation by arguments

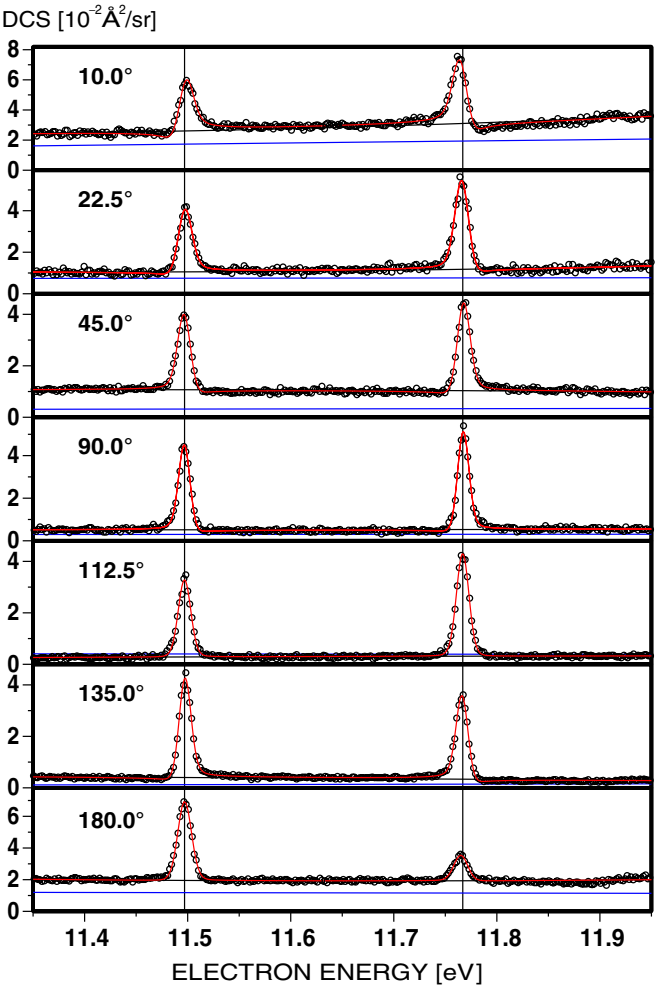

Figure 10. DCS for vibrational excitation to (X, $v = 1$) via (R, $v = 0,\ 1$). Data points: measurements with the FR apparatus; full (red) curves: least squares fits using equation (2), $\Gamma = 1.38$ meV; thin (blue) lines: non-interfering background σ_{bg}; thin (black) lines: total background σ_{nr}. (Colour online.)

based on the model previously used by Comer and Read and detailed out for $\theta = 18°$. All these effects are more clearly visible in the new results shown in figure 10.

In order to explore the potential of the model for a consistent description of elastic and vibrational excitation scattering, we derive fits for the DCS of figure 10 under the restriction that Γ is held fixed at the value determined from the elastic DCS and the factors $t(v_R)$ are taken from table 5. Besides ΔE, the resonance positions are carefully readapted in order not to spoil the small asymmetries. These fits are shown in figure 10 as full curves. Again, they appear to be perfect.

The parameters describing the resonance peaks, σ_{nr}, $\Delta\sigma$ and β for each of the two peaks, $v_R = 0,\ 1$, are then expressed in terms of a common $p(\theta)$, but different nonresonant amplitudes. This is indeed possible with only small variations of the $a\,e^{-i\phi}$ between the two peaks. However, this implies accepting that $|a|^2/(4k_ik_f)$ is not any more equal to σ_{nr}, that means the background DCS has to be split into a part that interferes with the resonance and a part that does not. This is an extension of the model we did not consider for elastic

Table 5. Parameters of equations (1) and (2) for the vibrational excitation DCSs at 90°; resonance width $\Gamma = 1.38$ meV; DCS in 10^{-22-v_X} m^2 sr^{-1}.

$v_R\, v_X$	0 1	1 1	2 1	0 2	1 2	2 2	1 3	2 3
$t(v)$	−0.259	0.235	0.022	0.044	−0.099	0.049	0.022	−0.027
σ_{nr}	0.49	0.53	0.56	0.39	0.37	0.36	2.70	2.41
$\Delta\sigma$	26.24	33.07	0.91	5.53	42.23	14.46	14.74	53.99
$\beta - \pi$ (°)	−2.6	2.8	4.9	−7.3	1.6	−2.1	−13.9	4.4
σ_{pr}	32.25	27.23	0.25	8.16	42.65	10.64	23.93	39.38
σ_{bg}	0.33	0.39	0.33	0.30	0.04	0.36	1.63	1.58
$\phi - \pi/2$ (°)	−21.0	−29.6	−15.6	−26.3	78.4	15.8	−33.5	−31.2
p^2	1.47	1.47	1.47	1.30	1.30	1.30	1.56	1.56

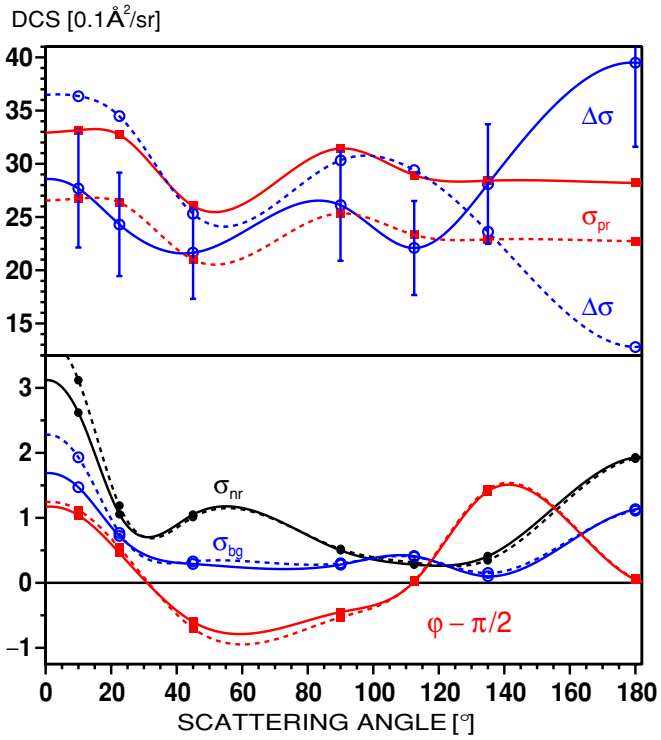

Figure 11. Analysis of the DCS for vibrational excitation: parameters of equations (2) and (3). Full curves: first peak (R, $v = 0$), dotted curves: second peak (R, $v = 1$). σ_{bg}: non-interfering background.

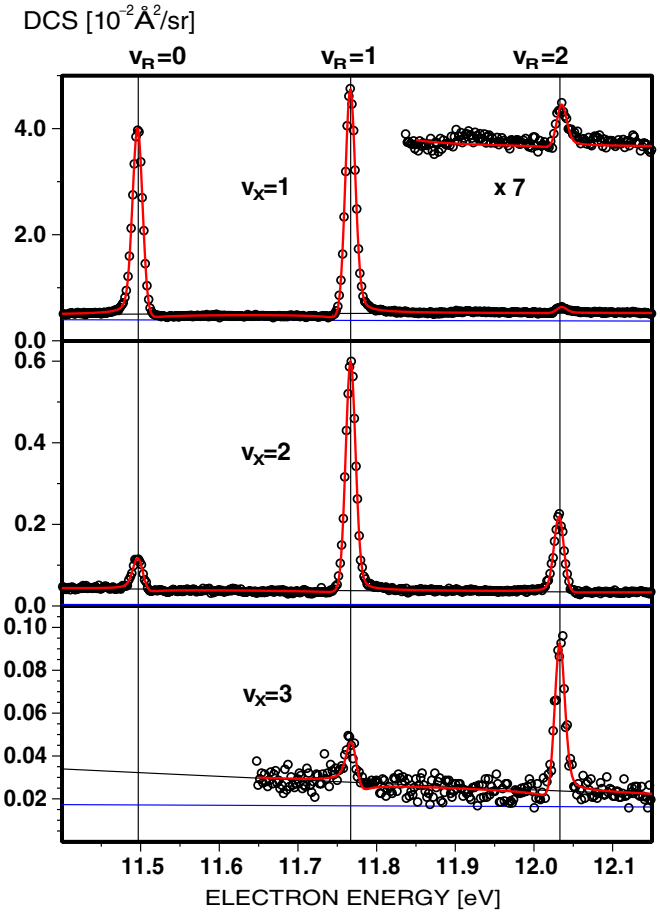

Figure 12. DCS at 90° for vibrational excitation to (X, v) via (R, v). Data points: measurements with the FR apparatus; full (red) curves: least squares fits using equation (2); thin (blue) lines: non-interfering background σ_{bg}; thin (black) lines: total background σ_{nr}. (Colour online.)

scattering. The opposite signs of the (small) asymmetries as well as the inversion of the ratios of peak areas from 1.2 to 0.8 are nicely accounted for by the change of sign of the vibrational factor $t(v)$ from the first peak to the second. The collapse of the second peak, starting somewhere below 135° and nearly complete at 180°, is traced to a sign change of $a\cos(\phi)$ followed by a rather steep increase. Apart from this backward region, the function $\phi(\theta)$ turns out quite similar to that for elastic scattering. The parameters as functions of θ are displayed in figure 11. $\Delta\sigma$ is shown with error bars indicating the uncertainties introduced by the experimental uncertainties of σ_{nr} of about 20%. To within these limits, σ_{pr} appears isotropic. Angular integration of $p(\theta)^2/2$ leads to a value of 1.30 instead of unity, marginally within the confidence range of the experimental data.

Further support for our model description of the resonance line profiles comes from data for higher vibrational excitation, $\Delta v = 2, 3$, measured at $\theta = 90°$. The nonresonant backgrounds are much stronger than an estimate for direct vibrational excitation as given above for $\Delta v = 1$ would predict, probably indicating that far wings of other resonances contribute significantly. The measured DCS are shown in figure 12, again with the fitting line which is obtained as just described. The alternation of the (very weak) asymmetries follows the sign changes of $t(v_R)$ within the peak sequence of the same v_X; $a\cos(\phi)$ is nearly constant for $v_X = 1, 3$, only for $v_X = 2$ the relative size of the peaks requires

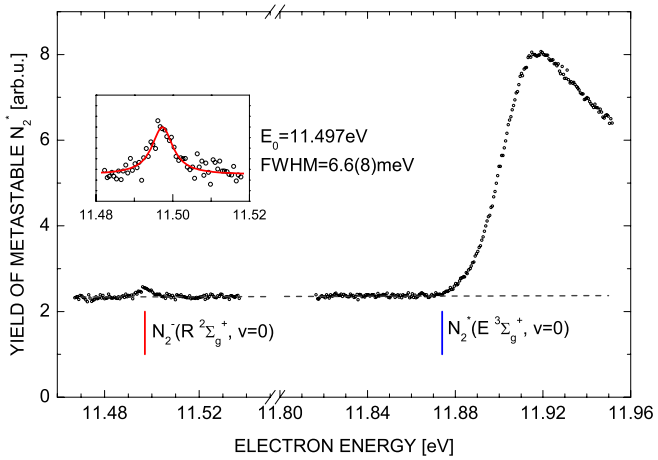

Figure 13. Yield for the production of metastable N_2^* molecules (see the text).

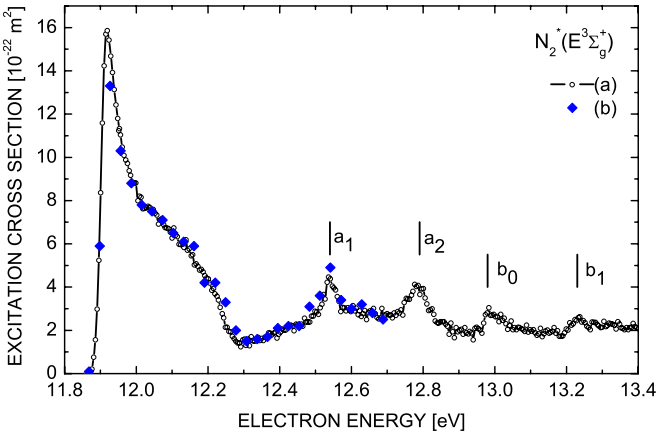

Figure 14. Excitation function for the production of metastable N_2^* molecules normalized to the absolute measurements of Brunger *et al* [39]. (a) Present work and (b) from [39].

$a\cos(\phi)$ to change sign. Values of the pertinent parameters are collected in table 5. $p(\theta)^2$ cannot be controlled by angular integration, but its particular value at 90° indicates—within the uncertainties of the measurement—a nearly isotropic scattering. In conclusion, it is clear that differences in peak heights by 2 orders of magnitude are nicely determined by vibrational transition moments with the help from the interference with a weakly varying nonresonant background. This nonresonant background may be caused or at least enhanced by the wings of neighbouring broad resonances (see figure 9).

5.4. Cross section for excitation of the metastable $N_2^*(E^3\Sigma_g^+)$ *level*

Using the off-axis channel electron multiplier of the KL setup for detecting long-lived excited species (see figure 1), the yield for the production of metastable levels of the N_2 molecule was investigated from 11.4 eV to 13.4 eV. Figure 13 shows the yield measured over two limited energy ranges around the $N_2^-\left(R^2\Sigma_g^+\right)$ resonance and around the onset of the $N_2^*\left(E^3\Sigma_g^+, v=0\right)$ level (spectroscopic threshold 11.874 eV) [25]. The sharp, essentially symmetric peak reflects enhancement of the metastable yield through the $N_2^-\left(R^2\Sigma_g^+\right)$ resonance; a fit with a Lorentzian profile (FWHM 6.6 meV) indicates an experimental energy resolution of about 5.4 meV. By a direct comparison with the resonances seen in elastic scattering, it was found that this sharp feature peaks at an energy identical with the resonance energy of 11.497(2) eV, as calibrated with the $Ar^-(3p^54s^2\ ^2P_{3/2})$ resonance. This peak provides an accurate calibration of the energy scale for the excitation function of the $N_2^*\left(E^3\Sigma_g^+\right)$ state which rises from an onset identical with the spectroscopic threshold (to within 2 meV) to a rather sharp peak, located at 11.917(3) eV, only 43 meV above the threshold. Angle-differential measurements of the cross section for $N_2^*\left(E^3\Sigma_g^+, v=0\right)$ excitation by Mazeau *et al* [40] have shown resonances at 11.92(2) eV and 12.16(3) eV (these two values have been increased by 0.02 eV to correct for the fact that these authors used for their energy calibration a value for the $He^-(1s2s^2\ ^2S_{1/2})$ resonance which is 0.02 eV below the now accepted value of 19.365(1) eV [15]). These two resonances have been classified as $^2\Sigma_u^+$ by Mazeau *et al* [40] according to the observed angular distribution. The prominent peak in the excitation function for $N_2^*\left(E^3\Sigma_g^+\right)$ at 11.917 eV appears to draw its strength largely from this resonance, while the resonance at 12.16 eV is a part of the shoulder in the excitation function for the $N_2^*\left(E^3\Sigma_g^+\right)$ state (see figure 14).

The nearly energy-independent metastable yield below the $N_2^*\left(E^3\Sigma_g^+\right)$ threshold and around the $N_2^-\left(R^2\Sigma_g^+\right)$ resonance is due to the excitation of lower-lying metastable levels (mainly $A^3\Sigma_u^+$ and $a^1\pi_g$ [10, 39, 41]). The dashed line in figure 13 represents a linear (almost constant) function fitted to this smooth yield. In order to derive a relative cross section for excitation of the $N_2^*\left(E^3\Sigma_g^+\right)$ state we consider this fit function to also serve as a proper extrapolation to higher energies (for a justification of this assumption, see [39]) and subtract it from the total metastable signal. The resulting cross section for excitation of the $N_2^*\left(E^3\Sigma_g^+\right)$ level is shown in figure 14. Its absolute scale is taken from the work of Brunger *et al* [39] by normalizing our yield to their absolute cross section (shown by diamonds) at energies around 12.1 eV. Very good overall agreement is observed between the shape of our cross section and that of Brunger *et al* . At the maximum of the threshold peak our cross section is 20% higher than that of Brunger *et al* probably as a result of our improved resolution. In view of the general interest in this cross section [39], we present numerical data for the threshold peak in table 6.

The excitation function of the $N_2^*\left(E^3\Sigma_g^+\right)$ state has been studied many times in the past. Here we only mention previous work carried out with high-resolution (energy width around 20 meV) [10, 39, 41]. Brunt *et al* [41] and Brunger *et al* [39] used similar setups involving a channel electron multiplier as the detector for the metastable levels. In order to enhance detection of low-lying metastable levels, Newman *et al* [10] applied a detector with heated tantalum ribbons in conjunction with a channel electron multiplier. As compared to our data (figure 13), the 'background' below the onset for $N_2^*\left(E^3\Sigma_g^+\right)$ excitation was substantially higher in the previous work. In

Table 6. Cross section for excitation of the $N_2^*(E^3\Sigma_g^+)$ state in 10^{-22} m^2; our data have been normalized to that of Brunger *et al* [39] around an energy of 12.09 eV.

E (eV)	ICS	E (eV)	ICS	E (eV)	ICS
11.871	0	11.934	13.9	12.045	7.5
11.876	0.2	11.939	13.1	12.069	7.2
11.881	0.8	11.943	12.4	12.083	6.8
11.886	1.6	11.948	11.8	12.093	6.7
11.891	3.0	11.953	11.3	12.102	6.5
11.895	5.2	11.958	10.9	12.121	6.0
11.900	8.4	11.963	10.2	12.150	5.6
11.905	11.6	11.973	9.6	12.179	5.0
11.910	14.2	11.982	9.2	12.198	4.5
11.915	15.7	11.992	8.9	12.217	3.7
11.920	15.9	12.001	8.5	12.237	3.0
11.924	15.4	12.011	8.2	12.256	2.1
11.929	14.7	12.021	7.7	12.275	1.7

the measurements of Brunt *et al* and Brunger *et al*, it had about the same size as the yield for the threshold peak near 11.92 eV. In the yield function of Newman *et al* , the threshold peak for $N_2^*(E^3\Sigma_g^+)$ excitation is much less prominent; it amounts to only about 9% of the total metastable yield.

The results of the earlier three studies agreed in the observation of resonance structure above 12 eV. In the range 12.4–13.4 eV, four peaks are observed and—following Mazeau *et al* [40]—these bands are labelled (a_1,a_2) and (b_0,b_1), as indicated in figure 14. These peaks have been associated with Feshbach resonances in which two outer valence electrons with antiparallel spins are attached to the $N_2^+(A^2\Pi_u)$ grand parent ion state. In our measurements, the maxima are located to within 10 meV at 12.54 eV (a_1), 12.79 eV (a_2), 12.98 eV (b_0) and 13.23 eV (b_1), respectively; these energies agree with those found in the previous work [40, 41, 10] within the mutual uncertainties. The peak heights of these structures exhibit some deviations (especially in [10]), which we attribute to different detector characteristics. We again emphasize the good agreement of our results with those of Brunger *et al* [39].

6. Conclusions

Using two electron scattering setups with resolutions ΔE of around 6 meV and 13 meV, respectively, the $N_2^-(R^2\Sigma_g^+)$ resonance has been characterized in detail by reporting DCS line profiles for the angular range 10°–180°. Elastic as well as vibrational excitation cross sections were put on an absolute scale by joining them to their absolute values from separate measurements at 11.4 eV. The position of the resonance was determined as 11.497(2) eV from simultaneous measurements of the $N_2^-(R^2\Sigma_g^+)$ and the lowest $Ar^-(4s^2)$ Feshbach resonance, and as 11.493 eV from *ab initio* calculations. The latter also gave accurate vibrational spacings and overlap integrals and provided details of the electronic structure of the resonance state.

The observed line profiles could be accurately represented by a Fano-type expression for the natural line profile, folded by a Gaussian to account for the respective apparatus resolution. However, even with the given high resolution, the electron energy width ΔE and the resonance width Γ could not be accurately determined separately: the fits turned out insensitive to their difference. Using the calculated overlap integrals, we derived a consistent interpretation of elastic and inelastic profiles as the result of interference between the resonant channels and single nonresonant backgrounds. This model provides a link between absolute DCS and Γ which could thus be determined to 1.38 meV from the FR data and to 1.22 meV from the KL data. These values imply that their nonresonant DCS at 11.4 eV are both scaled to the same absolute value. This may not be fully justified since the two setups discriminate differently against a possible background from rotational excitation—our tentative explanation of the difference. Our recommended value for the resonance width is 1.3(2) meV.

The (unexpected) features of vibrational excitation peaks with respect to their size and asymmetry could be linked to the signs of the pertinent overlap integral products. In this way, the experimental information is reduced to the parametrization of a background amplitude which is only weakly dependent on energy but shows a very characteristic variation of its phase with scattering angle. Its understanding requires a full scattering calculation which was not attempted here.

Acknowledgments

This work has been supported by the Deutsche Forschungsgemeinschaft (grant Ho427/28), by the 'Forschungszentrum Optische Technologien und Lasergesteuerte Prozesse', by the European Science Foundation through the network EIPAM ('Electron-Induced Processing At the Molecular level' Exchange grant no. 1288), and by the Swiss National Science Foundation (project no. 200020-113599). We thank D Spelsberg for help with the *ab initio* calculations and J Bömmels and A Gopalan for their experimental contributions in the early phase of this project. We gratefully acknowledge I Linert and M Zubek for providing data in numerical form.

References

[1] Heideman H G M, Kuyatt C E and Chamberlain G E 1966 *J. Chem. Phys.* **44** 355
[2] Comer J and Read F H 1971 *J. Phys. B: At. Mol. Phys.* **4** 1055
[3] Mulliken R S 1957 *The Threshold of Space* (Oxford: Pergamon)
[4] Kisker E 1972 *Z. Phys.* **257** 51
[5] Mazeau J, Gresteau F, Hall R I, Joyez G and Reinhardt J 1973 *J. Phys. B: At. Mol. Phys.* **6** 862
[6] Sanche L and Schulz G J 1972 *Phys. Rev.* A **6** 69
[7] Golden D E, Burns D J and Sutcliffe V C 1974 *Phys. Rev.* A **10** 2123
[8] Schulz G J 1973 *Rev. Mod. Phys.* **45** 423
[9] Brunt R J V and Gallagher A 1978 *Electronic and Atomic Collisions, ICPEAC X, Paris 1977* ed G Watel (Amsterdam: North-Holland)
[10] Newman D S, Zubek M and King G C 1983 *J. Phys. B: At. Mol. Phys.* **16** 2247
[11] Tremblay D and Roy D 1991 *J. Phys. B: At. Mol. Opt. Phys.* **24** 1867

[12] Mielewska B, King G C, Read F H and Zubek M 1999 *Chem. Phys. Lett.* **311** 428
[13] Read F H and Channing J M 1996 *Rev. Sci. Instrum.* **67** 2372
[14] Gopalan A, Leber E, Bömmels J, Paul S P H, Allegrini M, Ruf M-W and Hotop H 2004 *Eur. Phys. J.* D **30** 163
[15] Gopalan A, Bömmels J, Götte S, Landwehr A, Franz K, Ruf M W, Hotop H and Bartschat K 2003 *Eur. Phys. J.* D **22** 17
[16] Bömmels J, Franz K, Hoffmann T H, Gopalan A, Zatsarinny O, Bartschat K, Ruf M-W and Hotop H 2005 *Phys. Rev.* A **71** 012704
[17] Franz K, Hoffmann T H, Bömmels J, Gopalan A, Sauter G, Meyer W, Allan M, Ruf M-W and Hotop H 2008 *Phys. Rev.* A **78** 012712
[18] Allan M 1992 *J. Phys. B: At. Mol. Opt. Phys.* **25** 1559
[19] Nickel J C, Zetner P W, Shen G and Trajmar S 1989 *J. Phys. E: Sci. Instrum.* **22** 730
[20] Allan M 2000 *J. Phys. B: At. Mol. Opt. Phys.* **33** L215
[21] Allan M 2005 *J. Phys. B: At. Mol. Opt. Phys.* **38** 3655
[22] Allan M 2007 *J. Phys. B: At. Mol. Opt. Phys.* **40** 3531
[23] Werner H-J *et al* 2008 MOLPRO 2008.1, a package of *ab initio* programs
[24] Huber K P and Herzberg G 1979 *Molecular Spectra and Molecular Structure IV. Constants of Diatomic Molecules* (New York: Van Nostrand Reinhold Company)
[25] Carroll P K and Doheny A P 1974 *J. Mol. Spectrosc.* **50** 257
[26] Comer J and Read F H 1971 *J. Phys. B: At. Mol. Phys.* **4** 368
[27] Shore B W 1967 *Rev. Mod. Phys.* **39** 439
[28] Fano U 1961 *Phys. Rev.* **124** 1866
[29] Andrick D 1973 *Adv. At. Mol. Phys.* **9** 207
[30] Burke P G 1965 *Adv. Phys.* **14** 521
[31] Gote M and Ehrhardt H 1995 *J. Phys. B: At. Mol. Opt. Phys.* **28** 3957
[32] Linder F and Schmidt H 1971 *Z. Naturforsch.* **26 a** 1603
[33] Sun W, Morrison M A, Isaacs W A, Trail W K, Alle D T, Gulley R J, Brennan M J and Buckman S J 1995 *Phys. Rev.* A **52** 1229
[34] Muse J, Silva H, Lopes M C A and Khakoo M A 2008 *J. Phys. B: At. Mol. Opt. Phys.* **41** 095203
[35] Linert I and Zubek M 2009 *J. Phys. B: At. Mol. Opt. Phys.* **42** 085203
[36] Isaacs W A and Morrison M A 1996 *Phys. Rev.* A **53** 4215
[37] Shyn T W and Carignan G R 1980 *Phys. Rev.* A **22** 923
[38] Sauter G and Meyer W 2009 unpublished
[39] Brunger M J, Teubner P J O and Buckman S J 1988 *Phys. Rev.* A **37** 3570
[40] Mazeau J, Hall R I, Joyez G, Landau M and Reinhardt J 1973 *J. Phys. B: At. Mol. Phys.* **6** 873
[41] Brunt J N H, King G C and Read F H 1978 *J. Phys. B: At. Mol. Phys.* **11** 173